Journal of Membrane Science 349 (2010) 405–410

Contents lists available at ScienceDirect

Journal of Membrane Science

journal homepage: www.elsevier.com/locate/memsci

Permeability–selectivity analysis for ultrafiltration: Effect of pore geometry

Dharmesh M. Kanani[a], William H. Fissell[b,c], Shuvo Roy[d], Anna Dubnisheva[c], Aaron Fleischman[c], Andrew L. Zydney[a,*]

[a] Department of Chemical Engineering, The Pennsylvania State University, University Park, PA 16802, United States
[b] Department of Nephrology and Hypertension, Cleveland Clinic, Cleveland, OH 44195, United States
[c] Department of Biomedical Engineering, Cleveland Clinic, Cleveland, OH 44195, United States
[d] Department of Biopharmaceutical Sciences, University of California, San Francisco, CA, United States

ARTICLE INFO

Article history:
Received 23 September 2009
Received in revised form 1 December 2009
Accepted 1 December 2009
Available online 6 December 2009

Keywords:
Ultrafiltration
Permeability
Selectivity
Protein

ABSTRACT

The effects of pore size on the performance of ultrafiltration membranes are fairly well understood, but there is currently no information on the impact of pore geometry on the trade-off between the selectivity and permeability for membranes with pore size below 100 nm. Experimental data are presented for both commercial ultrafiltration membranes and for novel silicon membranes having slit-shaped nanopores of uniform size fabricated by photolithography using a sacrificial oxide technique. Data are compared with theoretical calculations based on available hydrodynamic models for solute and solvent transport through membranes composed of a parallel array of either cylindrical or slit-shaped pores. The results clearly demonstrate that membranes with slit-shaped pores have higher performance, i.e., greater selectivity at a given value of the permeability, than membranes with cylindrical pores. Theoretical calculations indicate that this improved performance becomes much less pronounced as the breadth of the pore size distribution increases. These results provide new insights into the effects of pore geometry on the performance of ultrafiltration membranes.

1. Introduction

The effects of pore size on the performance characteristics of ultrafiltration membranes are fairly well understood [1]. Membranes with large pores tend to have high filtrate flux but low protein retention, with the reverse being true for membranes with small pores. Mehta and Zydney [2] developed an appropriate framework for comparing the performance characteristics of different ultrafiltration membranes based on a plot of the membrane selectivity (or separation factor) as a function of the membrane hydraulic permeability (L_p). The appropriate selectivity for conventional ultrafiltration processes is equal to the flux of solvent divided by the flux of the macromolecule to be retained, which is simply equal to the reciprocal of the macromolecule sieving coefficient (S_a). Experimental data for the ultrafiltration of bovine serum albumin using a wide range of ultrafiltration membranes were used to highlight the trade-off between permeability and selectivity [2]. Model calculations performed by treating the membranes as a parallel array of cylindrical pores were in good agreement with the experimental data, clearly demonstrating the importance of hydrodynamic interactions in governing the overall performance of these ultrafiltration membranes.

Recent developments in materials science and nanotechnology have provided novel techniques for controlling not only the pore size and pore size distribution but also the pore geometry [3,4]. Chandler and Zydney [5] showed that the initial rate of flux decline during yeast cell microfiltration was reduced for membranes with slit-shaped pores compared to membranes with circular pores, with the difference in fouling behavior arising because the deposited cells are unable to fully block the slit-shaped pores due to their high aspect ratio. Worrel et al. [6] found higher flux and reduced fouling rates during microfiltration of silicon dioxide and polystyrene particles through poly(ethylene teraphthalate) track-etched membranes that were stretched to generate ellipsoidal pores (compared to the cylindrical pores in the unstretched membranes), with the increased flux in good agreement with simple theoretical calculations based on an appropriate sieve mechanism [7]. However, there are currently no experimental data on the possible effect of the membrane pore geometry on the performance of ultrafiltration membranes, largely because of the difficulty in fabricating nanometer-size pores using traditional production techniques.

The objective of this paper was to examine the effect of the pore geometry on the trade-off between the permeability and selectivity of ultrafiltration membranes. Experimental data are

* Corresponding author. Tel.: +1 814 863 7113; fax: +1 814 865 7846.
E-mail address: zydney@engr.psu.edu (A.L. Zydney).

0376-7388/$ – see front matter © 2009 Elsevier B.V. All rights reserved.
doi:10.1016/j.memsci.2009.12.003

presented for both commercial ultrafiltration membranes and for novel silicon membranes with uniform slit-shaped nanopores fabricated by photolithography using a sacrificial oxide technique. Results are compared with theoretical calculations using available hydrodynamic models for solute and solvent transport through membranes composed of a parallel array of either cylindrical or slit-shaped pores. The results clearly demonstrate that membranes with uniform slit-shaped pores have higher performance, i.e., greater selectivity at a given value of the permeability, than membranes with uniform cylindrical pores. This improved performance decreases as the pore size distribution becomes broader due to the different dependence of the hydrodynamic hindrance factor on the characteristic pore size for membranes with slit and cylindrical pores.

2. Permeability–selectivity analysis

The permeability–selectivity analysis for ultrafiltration membranes has been discussed in some detail by Mehta and Zydney [2]. The analysis is developed for ultrafiltration of a large macrosolute, e.g., a protein, in which the goal is to remove water and buffer components. Since mass transport in ultrafiltration is dominated by pressure-driven convection, the flux of all solutes through the membrane is directly proportional to the ultrafiltration rate. Under these conditions, the selectivity (or the separation factor) is simply equal to the ratio of the sieving coefficient for the small buffer components to that of the macrosolute (protein):

$$\alpha = \frac{1}{S_a} \tag{1}$$

where the sieving coefficient of the small buffer component has been set equal to one due to the absence of any significant retention of such a small species.

The permeability of interest in ultrafiltration is that with respect to the solvent (typically water):

$$L_p = \frac{J_v}{\Delta P} \tag{2}$$

where J_v is the volumetric filtrate flux (volume flow rate per unit membrane area) and ΔP is the transmembrane pressure driving force. For membranes with a parallel array of uniform cylindrical pores, the permeability can be evaluated directly from the Hagen–Poiseuille equation as:

$$L_p = \frac{\varepsilon r_p^2}{8\mu\delta_m} \tag{3}$$

where ε is the membrane porosity (membrane pore area divided by membrane cross-sectional area), r_p is the pore radius, μ is the solution viscosity, and δ_m is the membrane thickness.

The selectivity can be expressed as a unique function of the scaled permeability (β) using the expression developed by Zeman and Wales [8] for the actual sieving coefficient of a macrosolute with radius a:

$$S_a = \left(1 - \frac{a}{\sqrt{8\beta}}\right)^2 \left[2 - \left(1 - \frac{a}{\sqrt{8\beta}}\right)^2\right] \exp\left(-\frac{0.0893a^2}{\beta}\right) \tag{4}$$

where the scaled permeability is defined as:

$$\beta = \frac{\mu L_p \delta_m}{\varepsilon} \tag{5}$$

According to Eq. (4), the selectivity of a membrane with uniform cylindrical pores becomes infinite (corresponding to $S_a = 0$) when

$$\beta^* = \frac{a^2}{8} \tag{6}$$

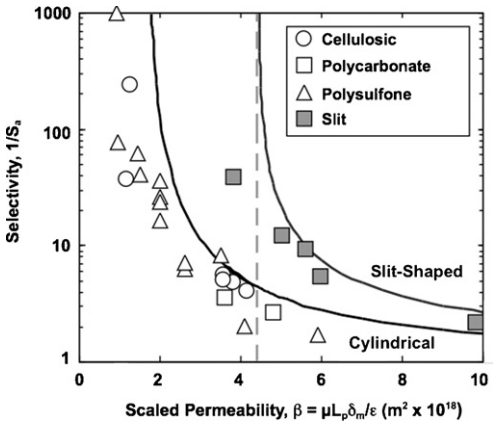

Fig. 1. Selectivity–permeability trade-off for ultrafiltration membranes using albumin as the model protein. Open symbols represent data for polymer ultrafiltration membranes. Filled symbols represent data for novel silicon membranes with nanometer-size slit-shaped pores as discussed in the text. The data point shown at $\beta = 9.8 \times 10^{-18}$ m^2 is actually at $\beta = 20 \times 10^{-18}$ m^2 but has been moved to accommodate the scaling of the figure. Solid curves represent model calculations for membranes consisting of a parallel array of uniform cylindrical or slit-shaped pores. The dashed vertical line is the permeability of a slit-pore membrane with infinite selectivity.

Note that the scaled permeability defined by Eq. (5) is a unique function of the pore size (and pore geometry) independent of the membrane thickness and the pore density since L_p varies linearly with the porosity and inversely with thickness.

Fig. 1 shows the selectivity–permeability trade-off for a series of ultrafiltration membranes using bovine serum albumin as a model protein. The literature results and sources are discussed in more detail by Mehta and Zydney [2]. In each case, the selectivity was evaluated using Eq. (1) with the actual protein sieving coefficient (S_a) calculated from experimental data for the observed sieving coefficients ($S_o = C_{filtrate}/C_{feed}$) using the simple stagnant film model [1]:

$$S_a = \frac{S_o}{(1 - S_o)\exp(J_v/k) + S_o} \tag{7}$$

The mass transfer coefficients (k) in the different modules were calculated using the correlations given by Zeman and Zydney [1]. The solvent viscosity was taken as that of water at the temperature of the experiments. The thickness of the asymmetric polysulfone, polyethersulfone, and cellulosic membranes was taken as $\delta_m = 0.5\,\mu$m (corresponding to the thickness of the skin layer of the membrane) with the porosity estimated as $\varepsilon = 0.5$. Although there is considerable uncertainty in the actual values of δ_m and ε for these asymmetric membranes, data for a variety of different membranes indicate that the ratio $\delta_m/\varepsilon \approx 1.0\,\mu$m [1]. The thickness and porosity of the track-etched polycarbonate membranes were 10 μm and 0.05, respectively. The error bars on the scaled permeability (not shown in Fig. 1) are around ±20% based on the uncertainties in the values of δ_m/ε. The use of the scaled permeability brings the results for the polycarbonate membranes into good agreement with the data for the asymmetric cellulosic and polysulfone membranes since this scaling properly accounts for the effects of both the membrane porosity and thickness on the ultrafiltration performance. The membranes with large values of the scaled permeability (corresponding to large pore size) have poor albumin retention and thus low selectivity as expected.

The solid curve in Fig. 1 labeled "Cylindrical" was developed directly from Eqs. (1) and (4) for a membrane with uniform cylindrical pores with the radius of BSA taken as $a = 3.65$ nm. The data for this wide range of membranes all tend to cluster slightly below and to the left of the theoretical curve. This is a direct result of the

detrimental effects of the pore size distribution on the trade-off between the selectivity and permeability as discussed by Mehta and Zydney [2]. It was possible to fit the experimental data to the model using a log-normal pore size distribution with the ratio of the standard deviation to the mean pore size equal to 0.2 [2]. The filled symbols in Fig. 1 represent experimental data obtained with novel silicon ultrafiltration membranes with uniform slit-shaped pores as discussed in the next section.

3. Materials and methods

Silicon membranes with uniform slit-shaped nanopores were fabricated from silicon substrates following the procedure outlined by Fissell et al. [9] and Lopez et al. [10]. Fabrication of membranes starts with a 400 μm-thick, 100 mm-diameter, double side polished ⟨1 0 0⟩-oriented silicon wafer that is obtained from a commercial vendor. The wafer was coated with a 500 nm-thick layer of low-stress silicon nitride followed by a 5 μm-thick film of polycrystalline silicon (polysilicon). The polysilicon layer was patterned by photolithography and reactive ion etching to create approximately 50 μm-long spaces and lines that are 2–3 μm wide. Thermal oxidation of the patterned polysilicon was performed to grow a thin conformal SiO_2 film that defines the eventual size of the nanopores. The thickness of this conformal SiO_2 film could be readily varied between 5 and 100 nm by adjusting oxidation parameters such as time and temperature. After deposition of another 4 μm-thick polysilicon film, chemical–mechanical polishing was performed to expose the nanopore regions on the front-side of the wafer. Low-stress silicon nitride was deposited on both front- and back-sides of the wafer, with the back-side patterned to define an etch mask. The wafer was subsequently etched in KOH to create suspended membranes. Finally, the masking silicon nitride and SiO_2 films were etched in concentrated hydrofluoric acid to produce nanoporous membranes with slit-shaped pores approximately 45 μm in length and 5–30 nm in half-width.

To minimize membrane fouling, the silica surface was modified by covalent attachment of poly(ethylene glycol) (PEG) using a previously reported solution phase method, but without the sonication steps and with the PEG deposition continued for 12 h [11]. The PEG was covalently coupled to the silanol groups (Si–OH) on the silicon surface through a trimethoxysilane group forming a Si–O–Si–PEG moiety. The wafers were subsequently cut into 1 cm × 1 cm chips for use in the ultrafiltration experiments. Membrane arrays were examined under differential interference contrast light microscopy for defects.

The hydraulic permeability of the silicon membrane was evaluated using phosphate buffered saline (PBS), with the flow rate measured by timed collection over a range of pressures from 3.4 to 13.8 kPa (0.5–2 psi). Sieving data were obtained using membranes mounted in an ultrafiltration cell. The retentate side of the membrane was continuously perfused at a flow rate of 1 ml/min from a 100 ml reservoir containing bovine serum albumin (Fraction V, Sigma Chemicals, Catalog Number, A5378, St. Louis, MO) at a concentration of either 50 or 4000 mg/l. The permeate side of the membrane was wet with a measured volume of PBS. Compressed dry air was used to generate a transmembrane pressure of 13.8 kPa (2 psi) as monitored by a pressure transducer (Entran, EPX 10PG, Les Clayes-sous-Bois, France) within the filtration cell. The ultrafiltration rate was determined by timed collection using a calibrated syringe barrel (Hamilton, Reno, Nevada, USA) capped with parafilm. Albumin concentrations in the feed and permeate samples were determined by Bradford assay (BioRad, Hercules, California, USA).

Sieving data were also obtained with 50 μg/ml polydisperse FITC-labelled Ficoll 70 (Sigma, St. Louis, MO, USA) prepared after the method of Ohlson et al. [12]. Permeate was collected at timed intervals using a 13.8 kPa (2 psi) applied pressure, corresponding to membrane fluxes of approximately 10^{-8} m/s. Feed and permeate samples were analyzed by gel permeation chromatography with a Waters Ultrahydrogel 500 column (for the Ficoll) or a Tosoh TSK-Gel 4000sw-xl column (for albumin) on a Waters 600E system using Waters 474 fluorescence and variable wavelength UV–vis detectors. Size calibration of the column was performed with monodisperse Ficolls of known sizes, which were the kind gifts of Dr. Bengt Rippe (Lund University) and Dr. William M. Deen (Massachusetts Institute of Technology).

4. Results and analysis

Fig. 2 shows typical scanning electron micrographs of the cross-sectional view of two different nanoporous silicon membranes. The inner surface of the pore is very smooth, consistent with the expected morphology of the smooth fine-grained polysilicon. Single pores are visible in both membranes, with the pore dimensions remaining constant through the entire depth of the silicon, i.e., over the entire pore length. The membrane pore size was determined directly from the SEM images, with the two membranes shown in Fig. 2 having slit half-widths of 17 and 7 nm (top and bottom panels, respectively).

The pore size characteristics of the silicon nanopore membranes were also examined by measuring the sieving coefficients of fluorescently labeled Ficoll at low filtrate flux, conditions where concentration polarization is negligible. The observed sieving coefficients are shown as a function of the ratio of the Ficoll radius

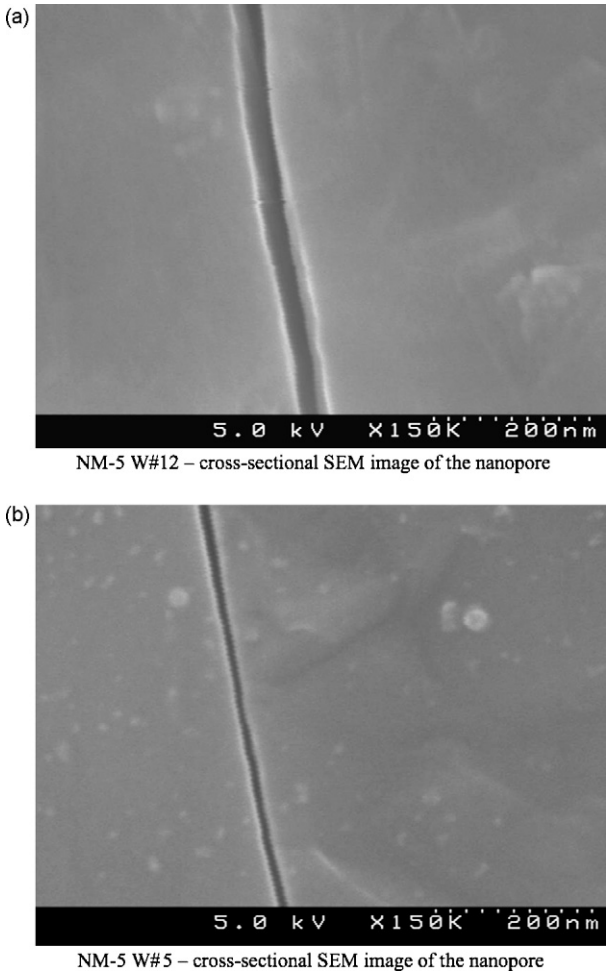

Fig. 2. Scanning electron micrographs of membranes with pore half-widths of $h = 17$ nm (top panel) and $h = 7$ nm (bottom panel).

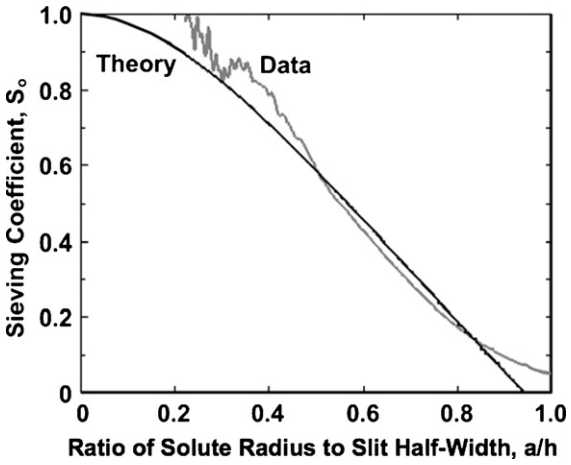

Fig. 3. Ficoll sieving coefficients as a function of the ratio of solute radius to pore slit half-width for a nanoporous silicon membrane with $h = 25$ nm. Theoretical calculations are described in the text.

(determined from size exclusion chromatography) to the pore slit half-width (h) in Fig. 3. Also shown for comparison are model calculations using the theoretical expression for the sieving coefficient in a slit-shaped pore developed by Dechadilok and Deen [14]:

$$S_a = 1 - 3.02(a/h)^2 + 5.776(a/h)^3 - 12.3675(a/h)^4 + 18.9775(a/h)^5 - 15.2185(a/h)^6 + 4.8525(a/h)^7 \quad (8)$$

where a is the solute radius. The data are in good agreement with the model, demonstrating that the behavior of the slit-pore membrane is consistent with theoretical predictions. The Ficoll sieving coefficients are somewhat greater than predicted at very large a/h, with $S_o = 0.05$ at $a/h = 1$. This could be due to the non-spherical nature of the Ficoll including the possible role of Ficoll deformation due to the converging flow into the pores as discussed elsewhere [15]. Alternatively, the non-zero sieving coefficient for the largest Ficolls could reflect the presence of a very small number of defects in the silicon membrane and/or to a small leakage flow around the membrane, although there was no independent evidence for either of these explanations.

The filled symbols shown previously in Fig. 1 represent experimental results for albumin sieving obtained with several different silicon membranes having different pore size (fabricated with different thickness of the sacrificial oxide layer). The albumin sieving coefficients were evaluated using both 50 and 4000 mg/l solutions; the results at the two protein concentrations were similar, with any small discrepancies reflecting the inherent uncertainties in the measurements. Shear rates in the feed compartment of the ultrafiltration cell were estimated to be $0.5\,s^{-1}$ at a feed flow rate of 1 ml/min. This corresponds to a Reynolds number (based on the channel height) of around $Re = 100$ and a mass transfer coefficient of approximately $k = 1.0 \times 10^{-7}$ m/s [13] as evaluated from the Leveque solution for fully developed channel flow [1]. The calculated mass transfer coefficient is about an order of magnitude larger than the ultrafiltration flux ($J_v \approx 10^{-8}$ m/s ≈ 0.04 L/m^2/h); thus, concentration polarization effects were negligible and $S_o \approx S_a$. The low value of the filtrate flux reflects the very low pore density of the silicon membranes (corresponding to a membrane porosity of $\varepsilon < 0.0006$).

The scaled permeability was calculated from the measured filtrate flow rate as a function of applied pressure using Eq. (5). The thickness of the silicon membrane was 4 μm. The porosity was estimated directly from the number of pores (N equal to 57,785 and 104,013 for the membranes examined in Fig. 1) with $w =$ 45 μm; the slit half-width was evaluated directly from the scanning electron micrographs assuming that the thickness of the PEG modification was 1 nm. The results for the slit-shaped pore membranes lie distinctly to the right of the data for the commercial ultrafiltration membranes, giving a marked enhancement in the trade-off between the selectivity and scaled permeability. Note that the data point plotted at $\beta = 9.8 \times 10^{-18}$ m^2 actually had about twice this permeability; the results were plotted at the smaller value of β so that the data point was visible on the plot in Fig. 1.

The solid curve labeled "Slit-Shaped" in Fig. 1 is developed in an analogous fashion to that used for the cylindrical pore membrane but with the hydraulic permeability and sieving coefficient evaluated for the slit-pore geometry. The hydraulic permeability is thus given as:

$$L_p = \frac{\varepsilon h^2}{3\mu\delta_m} \quad (9)$$

where h is the half-width of the slit. The selectivity was evaluated in terms of the scaled permeability using Eq. (8) with

$$h = \sqrt{3\beta} \quad (10)$$

based directly on Eqs. (5) and (9). The experimental data for the nanoporous silicon membranes are in fairly good agreement with the model calculations, consistent with the highly uniform pore structure generated by the lithographic technique. The data do lie somewhat to the left of the theoretical prediction, similar to the results for the polymeric membranes. The reason for this discrepancy is unclear, although it may simply be due to a reduction in membrane permeability arising from the presence of a small number of blocked pores.

The vertical dashed line in Fig. 1 represents the scaled permeability for a membrane with slit-shaped pores having infinite selectivity (corresponding to $S_a = 0$). This occurs when

$$\beta^* = \frac{a^2}{3} \quad (11)$$

which is 8/3 times the value for a membrane with cylindrical pores. This large increase in the scaled permeability is a direct result of the reduction in the hydrodynamic resistance to fluid flow provided by the rectangular (slit-shaped) pores compared to that for a membrane with cylindrical pores under conditions in which the critical pore dimension (either h or r_p) is equal to the size of the solute (a). This is due both to the smaller wetted perimeter per unit pore area in a slit-shaped pore compared to a cylindrical pore (δ_m/h versus $2\delta_m/r_p$) and to the differences in the detailed flow profiles in the cylindrical and Cartesian (slit-shaped) pores.

In order to examine the potential impact that a pore size distribution would have on the performance of these membranes, a series of calculations were performed for membranes having a log-normal pore size distribution [16]:

$$n(h) = \frac{n_0}{h\sqrt{2\pi}}\left[\ln\left(1 + \left(\frac{\sigma}{\bar{h}}\right)^2\right)\right]^{-1/2} \exp\left\{-\frac{(\ln(h/\bar{h})[1 + (\sigma/\bar{h})^2]^{1/2})^2}{2\ln[1 + (\sigma/\bar{h})^2]}\right\} \quad (12)$$

where $\bar{h}$ is the mean and σ^2 the variance of the distribution, respectively. The log-normal density function has been used extensively in the past to describe the pore size distribution of membranes having cylindrical pores [16]. The same distribution was used for membranes with slit-shaped and cylindrical pores with r and $\bar{r}$ replacing h and $\bar{h}$ in Eq. (12). The scaled permeability is then evaluated by appropriate integration of the corresponding expression

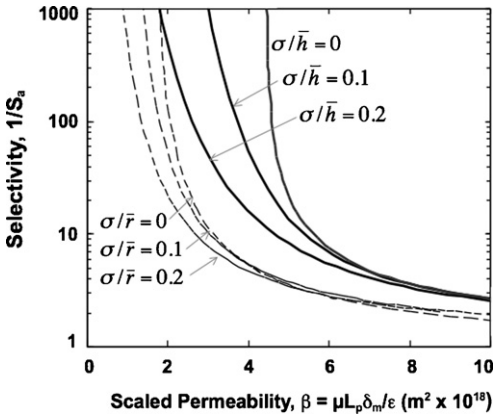

Fig. 4. Model calculations showing the influence of a membrane pore size distribution on the trade-off between selectivity and permeability for membranes with cylindrical and slit-shaped pores.

for the fluid velocity over the pore size distribution:

$$\overline{\beta} = \frac{1}{3}\frac{\int_0^\infty n(h)h^3\,dh}{\int_0^\infty n(h)h\,dh} \tag{13}$$

where the h^3 dependence in the numerator comes from the flow distribution, while the h dependence in the denominator is from the cross-sectional area of the slit-shaped pores ($A_{pore} = 2wh$). The selectivity is determined in a similar fashion by integrating the expression for $S_a(h)$ given by Eq. (8):

$$\overline{S_a} = \frac{\int_0^\infty n(h)S_a(h)h^3\,dh}{\int_0^\infty n(h)h^3\,dh} \tag{14}$$

Analogous expressions for membranes with a distribution of cylindrical pores are given in the literature [17].

The dashed and solid curves in Fig. 4 show simulations for membranes with cylindrical and slit-shaped pores, respectively, for different values of the coefficient of variation (ratio of standard deviation to the mean). As the coefficient of variation increases, the curve describing the selectivity–permeability trade-off moves down and to the left since the broader pore size distribution corresponds to a greater number of large pores that are non-retentive to the protein of interest. The shift in the trade-off curve is significantly more pronounced for the membrane with slit-shaped pores, which is a direct result of the lower hydrodynamic hindrance for protein convection in a slit pore compared to that in a cylindrical pore of the same critical dimension ($r_p = h$). For example, a slit pore with $h = 1.2a$ is predicted to have a sieving coefficient of $S_a = 0.17$ while a cylindrical pore with $r_p = 1.2a$ gives a sieving coefficient of only $S_a = 0.033$. Note that the performance of a membrane with slit-shaped pores having $\sigma/\bar{h} = 0.2$ remains greater than that for a cylindrical pore membrane with perfectly uniform pores ($\sigma/\bar{r} = 0$) for selectivity below 1000, although further increases in the breadth of the pore size distribution would lead to a reduction in performance compared to that for a membrane with uniform (monodisperse) cylindrical pores. Image analysis of the scanning electron micrographs of the silicon slit-pore membranes indicates that the coefficient of variation is typically less than 0.01; the model calculations using this value of $\sigma/\bar{h}$ would be indistinguishable from those for a membrane with perfectly uniform slit-shaped pores ($\sigma/\bar{h} = 0$) except at the very highest selectivities.

5. Conclusions

The results presented in this manuscript provide the first demonstration that ultrafiltration membranes with uniform slit-shaped pores can have significantly enhanced performance, as defined by the trade-off between the selectivity and permeability, compared to traditional ultrafiltration membranes that have cylindrical-shaped pores. This improved performance is a direct result of the reduced resistance to flow in a slit-shaped pore compared to that in a cylindrical pore of the same critical dimension ($r_p = h$). This effect was demonstrated experimentally using novel silicon membranes that have well-defined arrays of uniform slit-shaped pores, with the results in good agreement with theoretical predictions. Model calculations clearly show that pore size distribution has a greater effect on the performance of membranes with slit-shaped pores due to the larger value of the protein sieving coefficient in a slit pore having the same critical dimension as a cylindrical pore. Thus, the full advantage of using membranes with slit-shaped pores can only be realized if these membranes also have a relatively narrow pore size distribution, similar to what can be achieved with the nanoporous silicon membranes examined in this study.

It is important to note that the silicon membranes examined in this study have pore densities that are far too low for most practical applications ($\varepsilon < 0.0006$). In addition, the effective thickness of these membranes ($\delta_m = 4\,\mu m$) is considerably greater than the thickness of the skin layer of most asymmetric polymeric ultrafiltration membranes ($\delta_m = 0.5–1.0\,\mu m$). These parameters do not influence the results presented in Fig. 1 because the data have been plotted as a function of the scaled permeability (as defined by Eq. (5)), which properly accounts for differences in the membrane porosity and thickness. However, these factors would have a critical impact on the actual performance of the nanoporous silicon ultrafiltration membranes in any given application. Ongoing efforts are focused on increasing the pore density and reducing the thickness of these slit-pore membranes without sacrificing either their mechanical integrity or their highly uniform pore size.

Acknowledgements

This work was supported by grants: K08 EB003468 (National Institute of Biomedical Imaging and Bioengineering, NIH) and R01 EB008049-01 (National Institute of Biomedical Imaging and Bioengineering, NIH).

References

[1] L.J. Zeman, A.L. Zydney, Microfiltration and Ultrafiltration: Principles and Applications, Marcel Dekker, Inc., 1996.
[2] A. Mehta, A.L. Zydney, Permeability and selectivity analysis for ultrafiltration membranes, J. Membr. Sci. 249 (2005) 245–249.
[3] A.J. Bromley, R.G. Holdich, I.W. Cumming, Particulate fouling of surface microfilters with slotted and circular pore geometry, J. Membr. Sci. 196 (2002) 27–37.
[4] S. Kuiper, C.J.M. van Rijn, W. Nijdam, M.C. Elwenspoek, Development and applications of very high flux microfiltration membranes, J. Membr. Sci. 150 (1998) 1–8.
[5] M.C. Chandler, A.L. Zydney, Effects of membrane pore geometry on fouling behavior during yeast cell microfiltration, J. Membr. Sci. 285 (2006) 334–342.
[6] L.S. Worrel, J.A. Morehouse, L.A. Shimko, D.R. Lloyd, D.F. Lawler, B.D. Freeman, Enhancement of track-etched membrane performance via stretching, Sep. Purif. Technol. 53 (2007) 71–80.
[7] P.L. Hanks, C.A. Forschner, D.R. Lloyd, Sieve mechanism estimations for microfiltration membranes with elliptical pores, J. Membr. Sci. 322 (2008) 91–97.
[8] L.J. Zeman, M. Wales, Polymer solute rejection by ultrafiltration membranes, in: A.F. Turbak (Ed.), Membranes: Vol. II. Hyperfiltration and Ultrafiltration Uses, American Chemical Society, Washington, DC, 1981, ACS Symposium Series No. 54.
[9] W.H. Fissell, S. Manley, A. Westover, H.D. Humes, A.J. Fleischman, S. Roy, Differentiated growth of human renal tubule cells on thin-film and nanostructured materials, Am. Soc. Artif. Intern. Organs J. 52 (2006) 221–227.
[10] C.A. Lopez, A.J. Fleischman, S. Roy, T.A. Desai, Evaluation of silicon nanoporous membranes and ECM-based microenvironments on neurosecretory cells, Biomaterials 27 (2006) 3075–3083.
[11] A. Papra, N. Gadegaard, N.B. Larsen, Characterization of ultrathin poly(ethylene glycol) monolayers on silicon substrates, Langmuir 17 (2001) 1457–1460.
[12] M. Ohlsson, J. Sörensson, B. Haraldsson, Glomerular size and charge selectivity in the rat as revealed by FITC-Ficoll and albumin, Am. J. Physiol. Renal Physiol. 279 (2000) F84–F91.

[13] W.H. Fissell, A. Dubnisheva, A.N. Eldridge, A.J. Fleischman, A.L. Zydney, S. Roy, High-performance silicon nanopore hemofiltration membranes, J. Membr. Sci. 326 (2008) 58–63.
[14] P. Dechadilok, W.M. Deen, Hindrance factors for diffusion and convection in pores, Ind. Eng. Chem. Res. 45 (2006) 6953–6959.
[15] W.H. Fissell, S. Manley, A. Dubnisheva, J. Glass, J. Magistrelli, A.N. Eldridge, A.J. Fleischman, A.L. Zydney, S. Roy, Ficoll is not a rigid sphere, Am. J. Physiol.-Renal Physiol. 293 (2007) F1209–F1213.
[16] A.L. Zydney, P. Aimar, M. Meireles, J.M. Pimbley, G. Belfort, Use of the log-normal probability density function to analyze membrane pore size distributions: functional forms and discrepancies, J. Membr. Sci. 91 (1994) 293–298.
[17] S. Mochizuki, A.L. Zydney, Theoretical analysis of pore size distribution effects on membrane transport, J. Membr. Sci. 82 (1993) 211–228.